remote sensing

MDPI

Article

Temperature-Field Driven Adaptive Radiometric Calibration for Scan Mirror Thermal Radiation Interference in FY-4B GIIRS

Xiao Liang [1,2,3], Yaopu Zou [1,2,*], Changpei Han [1,2], Pengyu Huang [4], Libing Li [1,2] and Yuanshu Zhang [1,2,3]

[1] Shanghai Institute of Technical Physics, Chinese Academy of Sciences, Shanghai 200083, China
[2] State Key Laboratory of Infrared Physics, Shanghai Institute of Technical Physics, Chinese Academy of Sciences, 500 Yutian Road, Shanghai 200083, China
[3] University of Chinese Academy of Sciences, Beijing 100049, China
[4] School of Atmospheric Sciences and Guangdong Province Key Laboratory for Climate Change and Natural Disaster Studies, Sun Yat-sen University and Southern Marine Science and Engineering Guangdong Laboratory (Zhuhai), Zhuhai 519082, China
* Correspondence: zyp@mail.sitp.ac.cn

Highlights

What are the main findings?

- We elucidate the coupling between scan-mirror thermal emission and the instrument's polarization-dependent response during mirror deflection, quantitatively characterize the resulting interference, and establish a GIIRS-specific scan-mirror thermal-radiation interference model.
- Under strongly varying geostationary thermal environments, we establish a nonlinear mapping between the instrument thermal field and the interference term, thereby enabling adaptive modeling and real-time compensation.

What are the implications of the main findings?

- The correction uses only thermal-field data and scan-mirror angle status data to dynamically model and compensate, in real time, for scan-mirror thermal-radiation interference.
- This compensation suppresses biases induced by thermal-environment variability and scan-mirror deflection, significantly improving the continuity, accuracy, and long-term stability of radiometric calibration, thereby providing more reliable inputs for high-precision retrievals.

Abstract

To meet the growing demand for quantitative remote sensing applications in GIIRS radiometric calibration, this paper proposes a temperature field-driven adaptive scan mirror thermal radiation interference correction method. Based on the on-orbit deep space observation data from the Fengyun-4B satellite, this paper systematically analyzes the thermal radiation interference characteristics caused by scan mirror deflection and constructs the first scan mirror thermal radiation response model suitable for GIIRS. On the basis of this model, this paper further introduces the dynamic variation characteristics of the internal thermal environment of the instrument, enabling adaptive response and compensation for radiation disturbances. This method overcomes the limitations of relying on static calibration parameters and improves the generality and robustness of the model. Independent validation results show that this method effectively suppresses the interference of scan mirror deflection on instrument background radiation and enhances the consistency of the deep space and blackbody spectral diurnal variation time series. After correction, the average system bias of the interference-sensitive channel decreased by 94%, and the standard

check for updates

Academic Editor:
Pablo Rodríguez-Gonzálvez

Received: 8 October 2025
Revised: 26 November 2025
Accepted: 4 December 2025
Published: 6 December 2025

Citation: Liang, X.; Zou, Y.; Han, C.; Huang, P.; Li, L.; Zhang, Y. Temperature-Field Driven Adaptive Radiometric Calibration for Scan Mirror Thermal Radiation Interference in FY-4B GIIRS. *Remote Sens.* **2025**, *17*, 3948. https://doi.org/10.3390/rs17243948

Copyright: © 2025 by the authors. Licensee MDPI, Basel, Switzerland. This article is an open access article distributed under the terms and conditions of the Creative Commons Attribution (CC BY) license (https://creativecommons.org/licenses/by/4.0/).

deviation of radiance bias from 2.5 mW/m^2·sr·cm^{-1} to below 0.5 mW/m^2·sr·cm^{-1}. In the O-B test, the maximum improvement in relative standard deviation reached 0.15 K.

Keywords: GIIRS; FTIR; radiometric calibration; quantitative remote sensing; adaptive correction; temperature-field driven; instrument background radiation; scan mirror

1. Introduction

The Geostationary Interferometric Infrared Sounder (GIIRS) onboard the Fengyun-4B satellite is a Fourier transform-based hyperspectral infrared remote sensing payload in geostationary orbit. This instrument can acquire spectral information of infrared radiation from the earth scene, which is used to retrieve key atmospheric parameters such as atmospheric temperature and water vapor profiles, vector wind fields, and atmospheric trace gases. It has significant application value in numerical forecasting and high-impact weather monitoring, and early warning [1,2].

To ensure the reliability of remote sensing data for operational applications, maintaining the high accuracy and long-term stability of radiometric calibration results is a fundamental prerequisite. Therefore, it is necessary to systematically identify and rigorously suppress various sources of radiometric calibration errors during both the development phase and on-orbit operation. During on-orbit observations, it was found that changes in the position of the deep space calibration source can cause a shift in the deep space observation spectral response, leading to inconsistencies in the instrument background radiation in the two-point calibration model. This inconsistency, caused by mechanical angular variations in the scan mirror, results in a noticeable discontinuity in the calibration results over time, further impacting the accuracy of remote sensing data.

A systematic mechanism analysis and model construction have been conducted in previous studies on the interference caused by scan mirror deflection. Scan mirror deflection refers to the change in the angle state of the scan mirror when switching the observation field of view. For example, the Atmospheric Infrared Sounder (AIRS) onboard the Aqua satellite found during thermal vacuum testing that scan mirror deflection causes system polarization response differences. This was effectively corrected by constructing an angle response model that includes the thermal radiation terms of the scan mirror, thus compensating for background radiation interference [3]. The Cross-Track Infrared Sounder (CrIS) identified calibration bias related to scan angle caused by the scene selection mirror (SSM) rotation. Based on multi-angle deep space observation data, parameters were extracted, and angle disturbance correction terms were introduced into the calibration model, thus completing the calibration [4]. Building on these ideas, the FY-3D High Spectral Infrared Atmospheric Sounder (HIRAS) introduced angle correction terms into the calibration process by combining deep space observation with field-of-view consistency analysis, improving radiometric calibration accuracy [5]. In addition, scan mirror thermal radiation interference is not unique to Fourier-transform spectrometers and is also prevalent in various imaging infrared payloads. For instance, the Geostationary Operational Environmental Satellite-8/9 (GOES) imager found that variations in the scan mirror emissivity with the incident angle led to brightness temperature striping in the east–west direction. Related studies have introduced scan angle correction terms and established a radiometric interference correction method [6]. The Moderate Resolution Imaging Spectroradiometer (MODIS) established a Response Versus Scan-angle curve through pre-launch ground testing for calibration correction [7–9]; the Visible Infrared Imaging Radiometer Suite (VIIRS) and the Advanced Geostationary Radiation Imager (AGRI) used quadratic function fitting to model

the relationship between system response and scan angle [10–12]; For the GOES-R/ABI thermal emissive bands, pre-launch measurements of the mirror reflectivity and the angle dependence of emissivity, along with the mirror temperature, were used to introduce angle-dependent radiation terms for interference compensation [13].

The above studies indicate that the scan mirrors and their subsequent optical systems of thermal infrared spectrometers exhibit significant angle-dependent optical response characteristics, which can become important factors leading to radiometric calibration errors if not adequately characterized and accounted for. However, existing methods often rely on pre-launch or on-orbit dedicated experiments to obtain calibration parameters, which have clear time and operational condition dependencies. For pre-launch dedicated experiment calibration methods, the instrument may experience changes in optical performance due to influences such as intense vibrations during the launch phase, rendering the pre-launch angle response curve no longer applicable to on-orbit conditions. For on-orbit dedicated experiment calibration methods, when the instrument's temperature field changes, the background interference caused by a unit scan mirror angle deflection, as derived from deep space scan experiments, also changes. If scan mirror temperature information is not introduced, it is difficult to reflect this change in a timely manner. For GIIRS, since the scan mirror temperature cannot be directly obtained, and the mirror temperature in geostationary orbit is particularly affected by the seasonal and short-term fluctuations in the temperature field, it is urgent to develop a correction strategy that adapts to changes in the temperature field and updates calibration parameters accordingly, to achieve timely and accurate compensation in orbit.

To improve the accuracy and stability of radiometric calibration for the GIIRS payload on the FY-4B satellite, this paper conducts a systematic study on the background radiation interference caused by scan mirror deflection. First, based on on-orbit deep space observation experiments, the impact of mirror angle changes on the system response is analyzed, and the formation mechanism is clarified. Secondly, correction terms are introduced within the two-point calibration framework to quantify the background disturbance caused by scan mirror deflection, and a corresponding correction model is constructed. Meanwhile, a consistency evaluation index, which is based on the diurnal variation in the internal calibration target spectrum, is proposed. Furthermore, for scan mirror temperature changes, a nonlinear mapping between the scan mirror surface temperature and the instrument's temperature field is established, and based on this, calibration coefficients are obtained, enabling adaptive calibration that relies solely on on-orbit temperature field telemetry and scan mirror deflection angles, thus reducing dependence on dedicated experiment parameters. Finally, quantitative verification is carried out using independent on-orbit data, confirming the effectiveness of the model's calibration.

2. Materials and Methods

Two-point radiometric calibration uses dual reference sources to determine the response function, effectively suppressing stable background components during the calibration period. However, under on-orbit conditions, scan mirror deflection and fluctuations in the instrument's temperature field can cause the background radiation to experience non-steady-state drift, introducing systematic biases that are difficult to eliminate with the two-point calibration method. Therefore, it is necessary to construct a scan mirror thermal radiation interference model, identify the main driving factors of the interference, and design a corresponding disturbance compensation mechanism to improve the robustness and accuracy of the calibration model under on-orbit conditions.

2.1. Two-Point Radiometric Calibration Mechanism

The GIIRS onboard the FY-4B satellite sequentially observes deep space (DS), the internal calibration target (ICT), and performs a line-by-line scan of the earth's radiation scene (ES) by coordinating the control of the east–west and north–south scan mirrors, achieving infrared radiometric calibration based on dual reference sources. The instrument's scene selection module consists of two pivot-mounted mirrors installed vertically, with the east–west mirror responsible for the "step-and-stare" scan in the east–west direction for each line, and the north–south mirror responsible for switching the field of view for each scan line of the east–west mirror. The two mirrors work in coordination to perform multi-line scanning of the observation area and introduce the earth's radiation scene into the main optical system. The main optical system consists of a large-aperture off-axis three-mirror telescope, primarily used for collecting and compressing the Earth's radiation scene. The incident light collected and collimated by the main optical system enters the Michelson interferometer for modulation. After modulation, the incident light wave forms a time-varying interference pattern, which is received by the infrared detector and converted into an interferometric signal (See Figure 1).

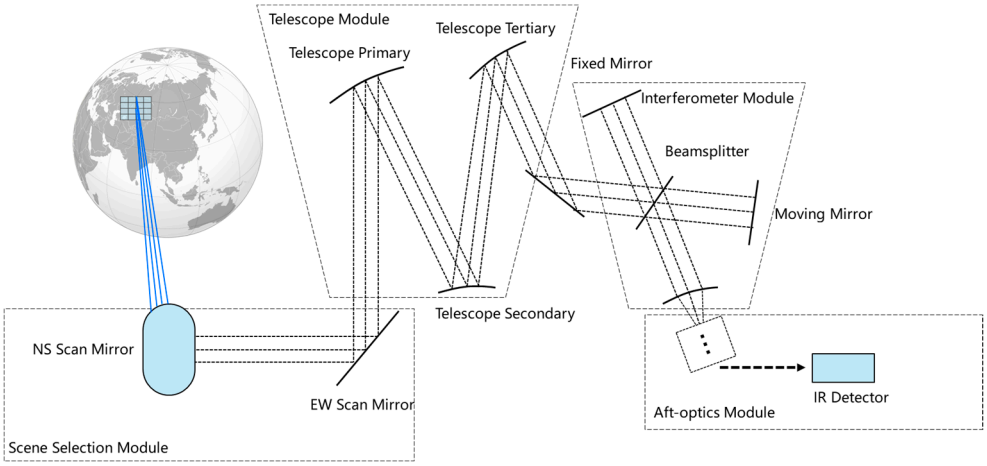


Figure 1. Main optical layout diagram of GIIRS.

Due to the complex optical structure of the GIIRS, the received signal not only contains external radiation from the main optical path, but also includes interference components from various internal thermal radiation sources within the system. Based on the differences in radiation sources and modulation paths, the interferometric signal received by GIIRS primarily consists of the following four components [14]: (1) External radiation from the main optical path: This originates from the observed target scene, enters the interferometer through the main optical path, and forms a modulated signal containing valid spectral information from the target. (2) Thermal radiation from the forward optical components: This originates from the thermal radiation of the optical components at the entrance of the interferometer (e.g., the scan mirror, collimating telescope). (3) Thermal radiation from the backward optical components: This radiation originates from the optical system at the exit end of the interferometer. Part of it directly enters the detector, forming a non-modulated direct current (DC) component, while a portion is re-modulated via the reverse path and returns to the interferometer. (4) Thermal radiation from internal interferometer components: This includes radiation from critical optical components such as beam splitters.

Among these classifications, except for the external radiation from the main optical path, the other signals are considered as instrument background radiation. By using a two-point calibration model, the stable components of the background radiation can be

removed through differencing, thereby recovering the radiance of the ES. The mathematical expression is as follows [15]:

$$S^{DS} = R \times \left(L^{DS} + L_0\right) \tag{1}$$

$$S^{ICT} = R \times \left(L^{ICT} + L_0\right) \tag{2}$$

$$S^{ES} = R \times \left(L^{ES} + L_0\right) \tag{3}$$

Here, L^{DS}, L^{ICT}, and L^{ES} represent the radiance of DS, ICT, and ES, respectively. S^{DS}, S^{ICT}, and S^{ES} are the corresponding scene system response spectra. L_0 represents the background radiation, and R is the system responsivity. Due to the extremely weak radiation from DS, S^{DS} can be used as an indicator for the system's background radiation, thereby dynamically monitoring the background interference characteristics of the remote sensing system. Equations (1) and (2) are solved simultaneously to obtain the system responsivity:

$$R = \frac{S^{ICT} - S^{DS}}{L^{ICT} - L^{DS}} \tag{4}$$

Furthermore, by combining Equations (1) and (3), the target radiance can be solved:

$$L^{ES} = \frac{S^{ES} - S^{DS}}{R} + L^{DS} \tag{5}$$

This calibration framework establishes the system response function using dual reference sources and can effectively compensate for the stable component of the background radiation. However, during actual on-orbit operation, background radiation varies under the influence of scan mirror deflection and thermal environment fluctuations, generating unstable components that cannot be removed by two-point radiometric calibration and thus introduce system bias. Therefore, there is an urgent need to establish a quantitative assessment model for background radiation interference, analyze the primary driving factors behind its variations, and design corresponding disturbance compensation mechanisms to enhance the robustness and accuracy of the calibration model in real-world environments. This will not only improve the physical reliability of infrared brightness temperature inversion but also lay the foundation for the generation of high-quality atmospheric parameter products.

2.2. Scan Mirror Thermal Radiation Interference Mechanism

On-orbit observations revealed that with changes in the deep space calibration source position, the calibration results exhibited significant discontinuities in the time dimension. Trace-back analysis showed that this discontinuity is mainly caused by spectral response shifts induced by scan mirror deflection, resulting in inconsistencies in the background radiation under different observation modes, introducing systematic errors into the calibration results, and thereby reducing the radiometric calibration consistency and quantitative accuracy of remote sensing spectra.

Specifically, scan mirror deflection modulates the intensity and directional distribution of its self-radiation in the main optical path and couples with the polarization response of the subsequent optical path [3]. The scan mirror can be approximated as an ideal opaque body, with the sum of its emissivity and reflectivity equal to 1 in any incident direction [16]. According to Fresnel's law, the emissivity of the scan mirror for s-polarized (perpendicular to the incident plane) and p-polarized (parallel to the incident plane) radiation components varies with different scan angles, causing the emission distribution of its self-radiation to have angle-dependent characteristics [17]. Furthermore, the transmittance of the subsequent optical components of the scan mirror is sensitive to changes in the

radiation polarization state, thereby further amplifying the system's response to scan angle variations [18].

Previous studies have established a system response model for scan mirror thermal radiation in spaceborne spectrometers [3]:

$$S_p = R \times \frac{B_s}{4}\left((t_{max} + t_{min})(\varepsilon_p + \varepsilon_s) + (t_{max} - t_{min})(\varepsilon_p - \varepsilon_s)cos(2(\theta - \alpha))\right) \quad (6)$$

In the Equation, B_s represents the Planck radiation corresponding to the current temperature of the scan mirror, t_{max} and t_{min} represent the major axis and minor axis of the system's transmittance polarization ellipse, respectively. ε_p and ε_s represent the emissivity of the scan mirror in the p-polarized and s-polarized directions, respectively. α is the system's polarization phase, and θ is the scan mirror angle.

Given that the scan angle range of GIIRS is only $\pm 5.1^\circ$, this paper performs a first-order Taylor expansion of the scan mirror thermal radiation response under the constraint of Equation (6), establishing a thermal radiation response model for the scan mirror applicable to GIIRS to quantitatively characterize the response shift caused by scan mirror deflection.

$$S_p(\theta_{ew}, \theta_{ns}) = R \times (B_{ew}(C_{ew1}\theta_{ew} + C_{ew0}) + B_{ns}(C_{ns1}\theta_{ns} + C_{ns0})) \quad (7)$$

In the Equation, S_p represents the scan mirror thermal radiation system response for the east–west and north–south scan mirrors at the angle state $(\theta_{ew}, \theta_{ns})$, B_{ew} and B_{ns} represent the Planck radiation of the east–west and north–south scan mirrors at the current scan mirror temperature, respectively. C_{ew1}, C_{ew0}, C_{ns1}, C_{ns0} are determined by the transmission characteristics related to the polarization of the main optical path. C_{ew1} and C_{ns1} are the scan angle coefficient terms, while C_{ew0} and C_{ns0} are constant terms.

From Equation (7), it can be seen that under the condition of stable system optical characteristics, the amplitude of the response change caused by scan mirror deflection is determined by the scan mirror surface temperature. When the mirror surface temperature is stable, the response variable corresponding to each unit of scan angle is approximately constant. Two-point calibration can effectively cancel the stable background component, thus eliminating the constant term in Equation (7). By considering only the system response variation caused by scan mirror deflection, the corresponding scan-mirror-related system bias can be removed. Based on this, this paper establishes a functional relationship between scan angle changes and response terms, enabling the quantitative characterization and systematic compensation of scan mirror thermal radiation interference.

Furthermore, assuming that the scan mirror surface temperature remains stable throughout the calibration period, let the changes in the east–west and north–south scan mirror angles be denoted as Δx and Δy, respectively (the mirror angle posture is uniformly represented as: east–west scan mirror angle, north–south scan mirror angle). Based on Equation (7), the system response term caused by scan angle changes, $f(\Delta x, \Delta y)$, can be expressed as:

$$f(\Delta x, \Delta y) = S_p(\Delta\theta_{ew}, \Delta\theta_{ns}) = C_1 \times \Delta x + C_2 \times \Delta y \quad (8)$$

where $C_1 = R \times B_{ew} \times C_{ew1}$ and $C_2 = R \times B_{ns} \times C_{ns1}$, are defined as the east–west scan mirror coefficient and north–south scan mirror coefficient, respectively, corresponding to the system response term caused by unit scan angle changes.

Based on the above scan mirror thermal radiation and polarization response coupling model, and combining Equation (5), the system response signal can be compensated for scan angle differences, correcting the system bias caused by scan mirror deflection, thereby

obtaining the system responsivity R_p with the scan mirror thermal radiation interference removed and the earth scene radiance L_p^{ES}:

$$R_p = \frac{S^{ICT} - S_p^{DS}}{L_{HBB} - L_{CBB}} \tag{9}$$

$$L_p^{ES} = \frac{S_p^{ES} - S_p^{DS}}{R_p} + L_{CBB} \tag{10}$$

In this Equation, $S_p^{ES} = S^{ES}(x_{ES}, y_{ES}) - f(\Delta x_{ES}, \Delta y_{ES})$ and $S_p^{DS} = S^{DS}(x_{DS}, y_{DS}) - f(\Delta x_{DS}, \Delta y_{DS})$ represent the Earth scene observed spectrum and deep space observed spectrum after scan angle difference compensation, respectively. Here, $S^{ES}(x_{ES}, y_{ES})$ and $S^{DS}(x_{DS}, y_{DS})$ are the raw observed spectra of the system under the corresponding scan mirror angle states (x, y).

3. Results

This section is based on the on-orbit deep space observation data from FY-4B/GIIRS, and conducts three aspects of research on the system bias caused by scan mirror deflection: (1) Interference Characteristics Identification: By using multiple scanning modes, the angular modulation response of scan mirror thermal radiation interference and the temperature field-driven characteristics are systematically analyzed. (2) Background Radiation Disturbance Analysis and Correction: The deep space spectrum disturbance amplitude is used to quantitatively characterize the strength of the scan mirror thermal radiation interference, and the model correction effect is verified. (3) Spectral Diurnal Variation Consistency Evaluation: Using the internal calibration target diurnal variation trend as a reference, the interference suppression effect of the model is evaluated under the ES, DS, and ICT observation modes.

3.1. Scan Mirror Thermal Radiation Response Experiment

Given that the radiation intensity of deep space is extremely low, the response of the detection system during deep space observation is primarily dominated by the instrument's self-generated thermal radiation. Therefore, by analyzing the deep space spectrum (DSS) variation with scan conditions, the response characteristics of the scan mirror thermal radiation can be extracted. To quantify and model the system bias introduced by scan mirror deflection, FY-4B/GIIRS designed and implemented an all-weather deep space observation mode to support on-orbit quantitative analysis and physical modeling of scan mirror thermal radiation interference.

This study is based on the deep space observation data acquired by GIIRS from 19 September to 11 October 2022 (covering the satellite's turn-around period), and conducts on-orbit analysis of the polarization coupling of scan mirror thermal radiation. To eliminate the impact of the scan strategy on the observations, experiments were conducted with various scanning schemes, using different mirror angle combinations (an example of a single cycle is shown in Figure 2). The experiment is conducted in two-hour cycles, during which temperature field distribution, ICT spectra (internal calibration target response), and DS spectra (deep space response at a fixed scan mirror angle) are obtained. In ES mode, the deep space observation is conducted sequentially according to the mirror angle sequence preset in Figure 2. This paper first conducts interference mechanism analysis and parameter identification using the FOV-73 detector, with results also applicable to other detectors in the full field of view. Finally, the model is validated and optimized based on measured data, forming a scan mirror thermal radiation polarization coupling interference correction scheme that can be embedded into the regular calibration process.

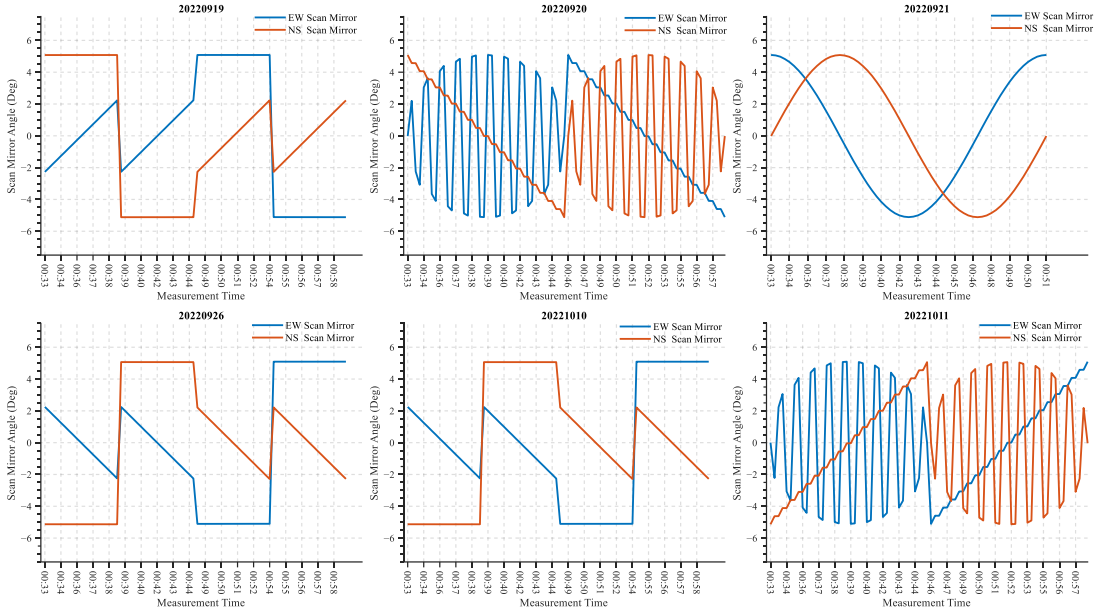


Figure 2. The motion trajectories of the east–west scan mirror (blue) and the north–south scan mirror (orange) over different days. The horizontal axis represents the observation time of a single cycle, and the vertical axis represents the scan mirror deflection angle.

3.2. Scan Mirror Thermal Radiation Interference Characteristics Analysis

To systematically characterize the scan mirror thermal radiation interference characteristics, this study first selects the deep space observation data acquired during the thermal steady-state operation period of the instrument (00:33–02:33), in order to effectively suppress the impact of temperature-field fluctuations on the system response. During this period, the temperatures of selected structural components of the instrument remain at relatively low levels, and the contribution of background radiation along the main optical path is relatively weak, thereby enhancing the detection sensitivity to the backward background radiation component along the main optical path and facilitating the identification of the composition characteristics of the system background radiation. Figure 3 illustrates the digital number (DN) response characteristics of the deep space spectrum corresponding to variations in the scan mirror angle during a single scan cycle. The observational results indicate that, for different experimental dates and scanning strategies, the DN values of the deep space spectrum decrease gradually with negative scan mirror deflection and change from positive to negative at a specific angle. Furthermore, a pronounced difference is observed in the distribution range of the deep space observation spectral DN values between the period before the satellite attitude adjustment (19–21 September 2022) and that after the adjustment (26 September–11 October 2022), indicating that the deep space observation response is jointly modulated by the scan mirror angle and the solar illumination conditions before and after the satellite attitude adjustment.

Results in Figure 3 indicate that scan mirror deflection changes the dominant radiation source of the background radiation. Because the scan mirror is located at the front end of the main optical path, its thermal radiation is directionally consistent with the propagation direction of the main optical path (i.e., it is phase-consistent). When the system response is positive, the dominant source of background radiation originates from the optical components in front of the interferometer along the forward optical path; when the scan mirror is negatively deflected and the system response turns negative, the dominant radiation source shifts to the optical components located in the backward optical path, whose propagation direction is approximately opposite to that of the main optical path. Therefore, negative deflection of the scan mirror can effectively reduce the relative contribution of its

own thermal radiation to the background radiation. This analysis provides guidance for optimizing the layout of the deep space calibration source and for designing correction strategies for scan mirror thermal radiation interference.

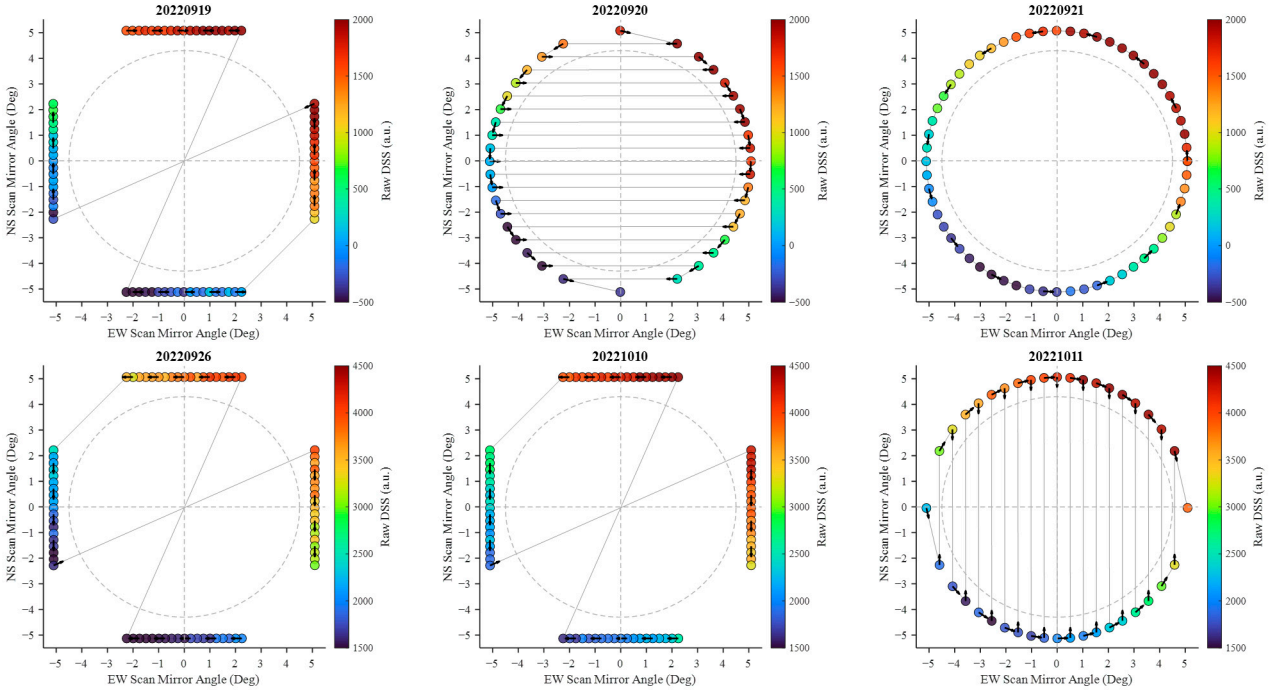


Figure 3. Distribution of deep space observation spectral DN with scan mirror deflection angle during a single scan cycle (729.53 cm^{-1}). The horizontal axis represents the east–west scan mirror deflection angle, and the vertical axis represents the north–south scan mirror deflection angle. The solid line represents the scan mirror motion trajectory, the arrows indicate the observation sequence direction, and the color scale represents the deep space DN response intensity. (Note: Some trajectories overlap during the scanning processes on 20 September and 10 October, and the overlapping trajectories are not shown in this figure. For details, please refer to Figure 1).

A comparison of the deep space responses on 19 September, 26 September, and 10 October 2022 in Figure 3 shows that, for two angle combinations with the same total negative deflection magnitude, (−2.2°, −5.1°) and (−5.1°, −2.2°), the combination in which the north–south scan mirror has the larger deflection exhibits a more pronounced decrease in DN. This indicates that the north–south scan mirror has a stronger capability to modulate the background radiation than the east–west scan mirror. The physical mechanism can be interpreted as follows: the thermal radiation from the north–south scan mirror must be reflected by the east–west scan mirror before entering the main optical path, so its angle variation not only changes the projection of its own radiation along the main optical path, but also modulates the incidence-angle conditions of the radiation onto the east–west scan mirror; in contrast, the thermal radiation from the east–west scan mirror is directly coupled into the main optical path, and its propagation path is relatively simple. Consequently, for a given unit angle deflection, the system response variation induced by the north–south scan mirror is larger than that induced by the east–west scan mirror. This effect is present not only in a single channel, but is also consistently confirmed over the wavenumber range 680.04–790.63 cm^{-1} shown in Figure 4.

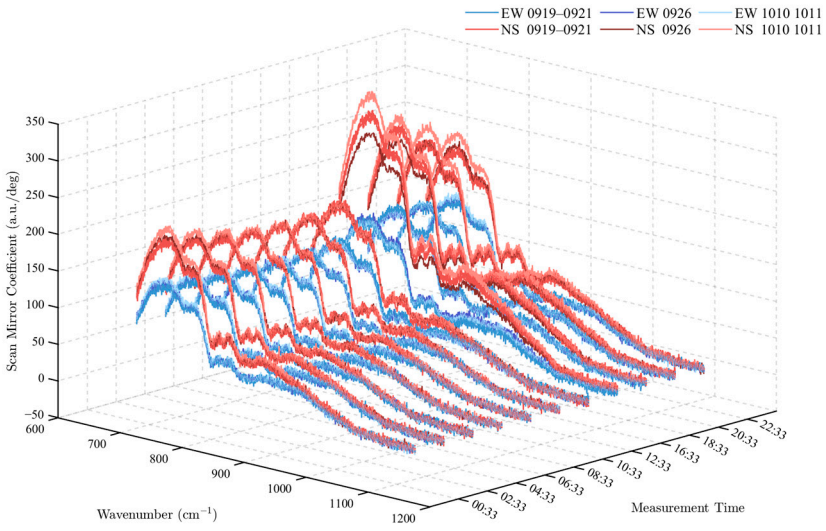


Figure 4. Diurnal variation trends of the east–west scan mirror coefficients and north–south scan mirror coefficients in the longwave channels from 19 September to 21 September 2022 (before attitude adjustment) and from 26 September to 11 October 2022 (after attitude adjustment). The solid lines in different colors represent the east–west scan mirror coefficients and north–south scan mirror coefficients for each observation date.

To further elucidate the scan mirror thermal radiation interference characteristics, all observation data acquired during the experiment period are used to quantitatively analyze the system response terms induced by unit scan mirror angle changes for all longwave channels, with particular emphasis on the variation characteristics of the east–west and north–south scan mirror coefficients and their driving factors (Figure 4).

The results in Figure 4 show that the scan mirror coefficients before and after the satellite attitude adjustment exhibit a clear commonality. First, the range of 680.04–790.63 cm^{-1} is the interference-sensitive wavelength band, where the effect of unit scan mirror angle change on the system output is particularly pronounced. Secondly, the east–west scan mirror and north–south scan mirror coefficients exhibit a stable diurnal variation pattern, reaching a peak after 16:33 each day, which is significantly higher than the values observed during the 00:33–12:33 period. Meanwhile, the scan mirror coefficients before and after the satellite attitude adjustment also show significant differences. Before the satellite attitude adjustment, the fluctuation range of the north–south scan mirror coefficient was relatively stable, with values remaining in the middle of the overall variation range. After the adjustment, the north–south scan mirror coefficients on different dates showed distinct grouping characteristics: on 26 September 2022, the values were lower than the pre-adjustment level, while on 10 and 11 October, they were higher than the pre-adjustment level.

To further identify the dominant factors affecting the variation in scan mirror thermal radiation interference intensity, a statistical analysis of the instrument's temperature-field characteristics is conducted. The results in Figure 5 show that the diurnal variation trend of the temperature field is highly consistent with the scan mirror coefficient in Figure 4, with both reaching a peak after 16:33 each day. Additionally, after the attitude adjustment, the overall temperature-field variation trend of the instrument synchronizes with the variation trend of the scan mirror coefficients. Correlation analysis quantitatively indicates a significant correlation between the temperature field and the scan mirror coefficients, with certain temperature measurement points showing strong indicative power for coefficient variation. A detailed analysis will be conducted in the following sections.

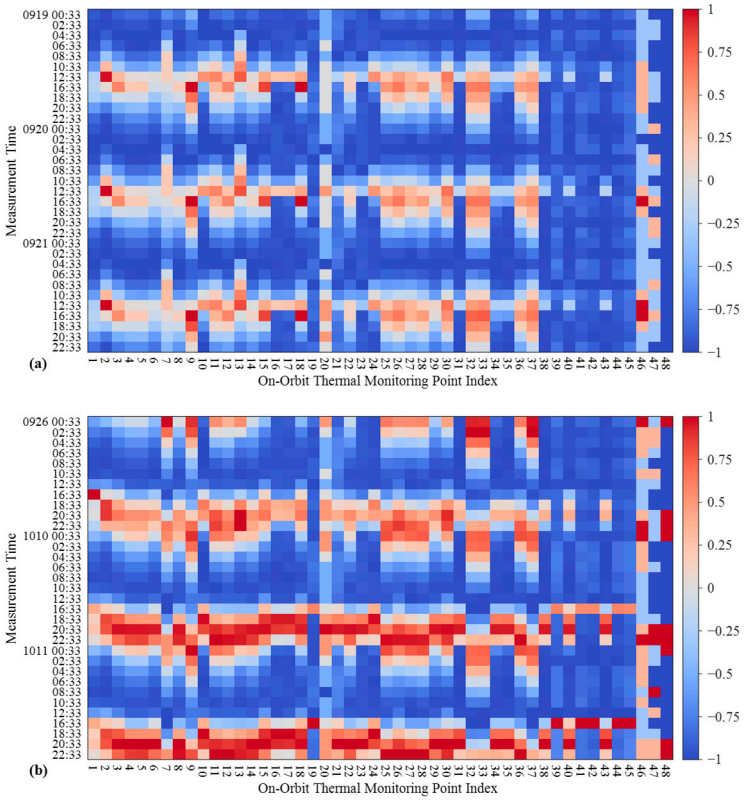


Figure 5. Diurnal variation characteristics of the 48 temperature measurement points on the instrument during the deep space observation period: (**a**) before the satellite turnaround; (**b**) after the satellite turnaround. The horizontal axis represents the temperature measurement point number, and the vertical axis represents the observation time. The color scale represents the normalized temperature value for each measurement point at the corresponding time.

According to Equation (7), the system response of scan mirror thermal radiation is primarily determined by the mirror surface temperature, the main optical path transmission characteristics, and the spectral responsivity. During the on-orbit operation, the latter two are relatively stable over short periods, making the mirror surface temperature the determining factor for changes in interference intensity. Specifically, on a daily scale, variations in solar irradiation conditions cause changes in the instrument's temperature field, which in turn drive fluctuations in mirror surface temperature, resulting in changes in the scan mirror thermal radiation interference intensity. Over the entire experimental period, satellite attitude adjustment leads to changes in solar incidence conditions, which collectively alter the instrument's temperature field and mirror surface temperature, thus causing changes in interference intensity. In summary, the instrument's temperature field can serve as a key physical parameter to characterize scan mirror thermal radiation interference, providing solid data support and a theoretical foundation for constructing a temperature-field-driven scan mirror thermal radiation interference prediction and compensation model.

3.3. Analysis of Background Radiation Perturbations

To quantitatively evaluate the interference effects caused by scan mirror deflection, the data from deep space observations with stable scan mirror angle changes on 21 September is selected as the analysis sample, in order to avoid the uncertainty interference caused by scan mirror attitude jumps. To improve the observation sensitivity of scan mirror thermal radiation interference, the data from the period of 16:33–18:33 on that day, when the temperature field was relatively high, is selected for analysis (the scan mirror angle changes are shown in Figure 2).

As shown in Figure 6a, the deep space spectrum with a fixed scan mirror angle of (−5.1°, 0°) under the DS observation mode is used as the instrument background radiation reference, and the background radiation interference caused by scan mirror deflection under the ES observation mode is quantitatively evaluated. The results show that at the high-sensitivity interference channel of scan mirror thermal radiation at 729.53 cm^{-1}, as the scan mirror angle in the ES observation mode changes from (2.99°, 4.09°) to (−1.58°, −4.89°), the background radiation interference caused by scan mirror angle changes accounts for approximately 78.82% of the baseline.

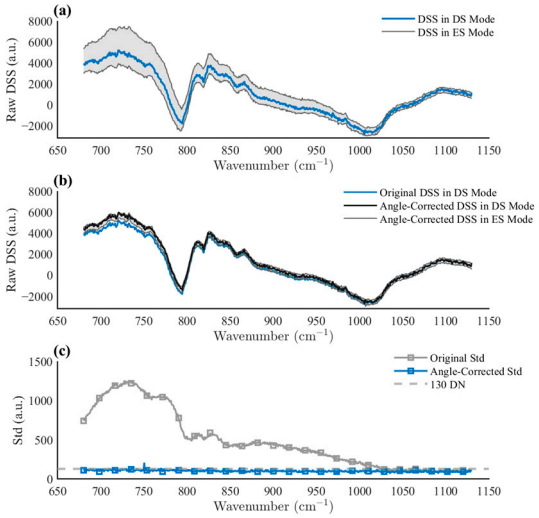


Figure 6. Deep space spectrum interference under different scan mirror angle states during the cycle: (**a**) The gray area represents the range of DN value changes in the deep space observation spectrum under different scan mirror angle states in the ES observation mode. The blue solid line represents the deep space observation spectrum in the DS observation mode under a fixed scan mirror angle state of (−5.1°, 0°). The vertical dashed line marks the position at 729.53 cm^{-1} on the horizontal axis. (**b**) The blue solid line is the same as in (**a**), representing the fixed deep space spectrum in the DS observation mode; the black solid line represents the deep space spectrum after scan angle difference compensation in the DS observation mode; the gray area represents the range of deep space spectrum variations after scan angle difference compensation in the ES observation mode. (**c**) The gray line represents the standard deviation of the original deep space spectrum in the ES observation mode, and the blue line represents the standard deviation of the deep space spectrum after scan angle difference compensation in the ES observation mode.

Based on the scan mirror coefficients obtained from Figure 4, the scan angle difference compensation is applied to the deep space spectra under different scan mirror angle states in both the ES and DS observation modes, bringing them to the unified mirror angle (0°, 0°) state. The correction results are shown in Figure 6b,c. After correction, the fluctuation range of the cold space spectra in the ES observation mode for all scan mirror angle states significantly converges. At 729.53 cm^{-1}, the maximum interference magnitude is significantly reduced from 78.82% to 7.7%, and the standard deviation is reduced from a maximum of 1260 DN to a stable level, maintaining below 130 DN. Additionally, Figure 6b shows that after correction, the deep space spectrum in the DS observation mode falls within the fluctuation range of the corrected spectrum in the ES observation mode, indicating that scan angle difference compensation can effectively improve background radiation stability and improve the data consistency across observation modes.

To further evaluate the scan mirror thermal radiation interference correction effect during all days of the experiment, Figure 7 shows that after the scan angle difference compensation, the fluctuations in deep space radiance bias are significantly reduced. After correction, the average radiance bias is steadily reduced from a maximum of 1 $mW/m^2 \cdot sr \cdot cm^{-1}$ to

0.06 mW/m^2·sr·cm^{-1}. Furthermore, the standard deviation of radiance bias is reduced from 2.5 mW/m^2·sr·cm^{-1} to below 0.5 mW/m^2·sr·cm^{-1}, effectively suppressing the response interference caused by scan mirror deflection.

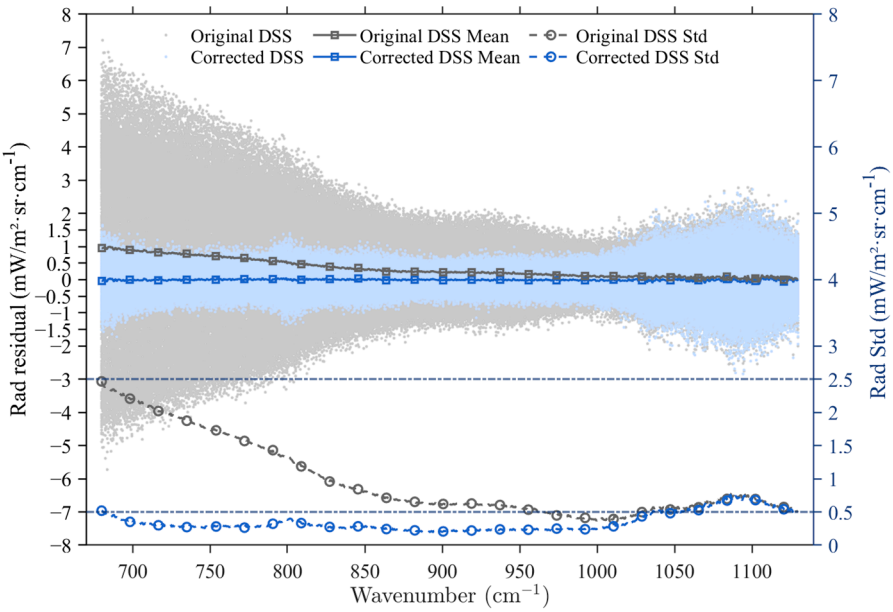


Figure 7. Scatter plot of deep space radiance bias before and after scan mirror thermal radiation interference correction during the deep space observation experiment period. The gray scatter points represent the radiance bias before correction, and the blue scatter points represent the radiance bias after correction. The gray solid line and blue solid line represent the average values of the radiance bias before and after correction, respectively. The gray and blue square markers represent the corresponding standard deviations.

3.4. Spectral Diurnal Variation Interference Analysis and Consistency Evaluation

After the correction of scan mirror thermal radiation interference, the fluctuation range of the instrument background radiation during the deep space observation experiment is significantly reduced. However, as shown in Figures 6b and 7, residual fluctuations still exist in the corrected deep space spectrum. The fundamental cause of this phenomenon lies in the continuous variation in the instrument's temperature field caused by changing solar irradiation conditions. The scan mirror thermal radiation interference correction model, established within a specific time window, cannot fully capture the complete characteristics of the background radiation variations with scan mirror angle during the entire observation cycle. Additionally, even with a fixed scan mirror angle, the instrument background radiation will still vary with changes in the temperature field, further exacerbating the temporal drift trend of the background radiation. Therefore, it is necessary to quantitatively characterize the diurnal variation in background radiation to verify whether the two-point calibration model established after the correction of scan mirror thermal radiation interference can effectively remove the background radiation component.

To address the above residual background radiation fluctuations, this paper conducts a quantitative evaluation of the consistency across different observation modes (ICT, DS, and ES) based on the temporal diurnal variation consistency of spectra. Given that the scan mirror angle is constant and the blackbody temperature is relatively stable in the ICT observation mode, the system response variations can serve as a reference for the true background radiation changes. Based on this, the on-orbit blackbody spectral diurnal variation is treated as the reference, and the spectral diurnal variation consistency before and after the scan mirror thermal radiation interference correction across different observation modes is analyzed. When the spectral diurnal variations in all observation

modes become consistent after correction, a two-point radiometric calibration model can be applied to compensate for the spectral diurnal variations in different observation scenes, thereby improving radiometric calibration accuracy and long-term stability. Meanwhile, the spectral diurnal variation consistency across different observation modes can serve as a quantitative indicator of the effectiveness of the scan mirror thermal radiation correction.

Based on the above evaluation system, this paper selects the two moments with the greatest differences in the scan mirror angle under the ES observation mode on a single day (06:40 and 16:47 on 21 September) for spectral diurnal variation consistency analysis. As shown in Figure 8a, at these two moments, the scan mirror angle in the ES observation mode changes from (0°, −5.14°) to (−3.44°, 3.78°), while the scan mirror angle in the DS observation mode changes from (−5.10°, −0.04°) to (5.08°, −0.01°). The results show that at the high-sensitivity interference channel of 729.53 cm^{-1}, the spectral diurnal variation bias in the ES observation mode relative to the true background radiation variation is 28.64%, while in the DS observation mode, the bias is 19.82%. After the scan angle difference compensation, as shown in Figure 8b, the disturbance amplitude in the ES observation mode is reduced to 5.94%, and in the DS observation mode, the disturbance amplitude is also reduced to 7.77%.

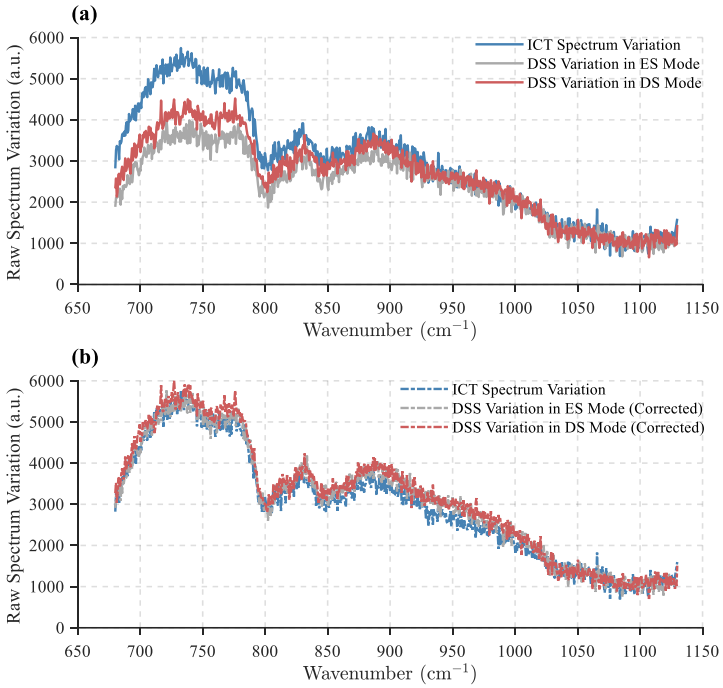


Figure 8. (**a**) Comparison of spectral diurnal variations for different observation modes at the two moments with the largest scan mirror state changes on 21 September (06:40 and 16:47) in the ES observation mode. (**b**) Spectral diurnal variation for different observation modes after standardizing the scan mirror angle. The blue solid line represents the spectral DN variation in the ICT observation mode, the gray solid line represents the spectral DN variation in the ES observation mode, and the red solid line represents the spectral DN variation in the DS observation mode. The spectra after removing scan mirror thermal radiation interference are shown as dotted lines.

To comprehensively evaluate the correction effect, further analysis was conducted on all observation data during the experiment. In the scan mirror thermal radiation interference sensitive wavelength band (680.04–790.63 cm^{-1}), the bias distribution characteristics of the deep space spectrum diurnal variation DN values were studied. As shown in Figure 9, there is a clear difference in the bias distribution characteristics before and after the correction. Before the correction, the bias mean was 530 DN, and the standard deviation was as high as 965 DN, indicating a significant systematic bias. After correction, the

bias mean was significantly reduced to −76 DN, and the standard deviation decreased to 457 DN. The error distribution significantly converged and approached zero, displaying an approximately Gaussian distribution pattern, with most of the data falling within the ±1σ range.

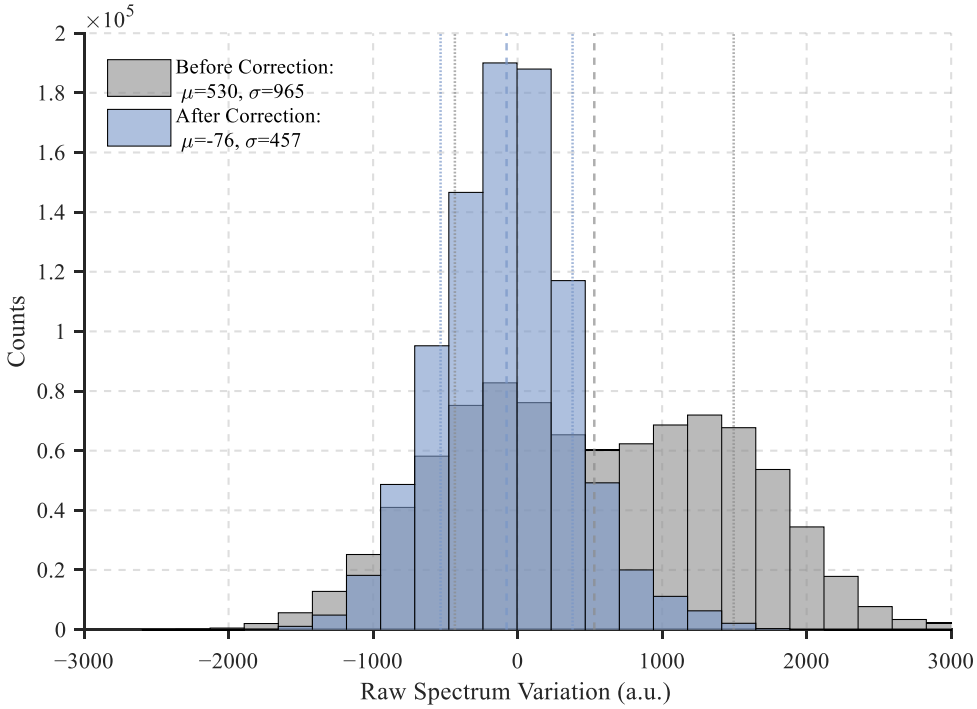


Figure 9. Error histogram of the bias between deep space spectral diurnal variation DN and blackbody diurnal variation DN in the frequency range of 680.04–790.63 cm^{-1} during the experiment period. The gray histogram represents the error distribution before correction, and the blue histogram represents the error distribution after correction. The gray dashed line and the blue dashed line represent the mean and ±1σ range before and after correction, respectively.

The above results indicate that the constructed correction model can effectively suppress the radiation disturbance introduced by scan mirror deflection and improve the spectral diurnal variation consistency across different observation modes. Additionally, statistical analysis further verifies that the systematic bias dominated by the scan mirror in the corrected background radiation has been effectively reduced.

3.5. Scan Mirror Deflection Induced Brightness Temperature Disturbance Analysis

Under the condition that the blackbody and Earth scene spectra remain unchanged, changing the position of the deep space reference source leads to significant differences in the calibration results (see Figure 10). In the deep space spectrum observation, when the scan mirror angle changes from (0°, −5.1°) to (0°, 5.1°), the calibrated ES brightness temperature exhibits a maximum jump of 3.98 K. After correction for the scan mirror thermal radiation, this value is reduced to 0.4 K. In the interference-sensitive wavelength band of 680.04–790.63 cm^{-1}, the average brightness temperature jump amplitude after correction is reduced from 1.31 K to −0.01 K. The above results indicate that the systematic bias caused by scan mirror deflection cannot be ignored. It should be noted that even though the scan mirror angle is fixed during the deep space observation phase, in the ES observation mode, the scan mirror angle for scanning the Earth scene still continuously changes with the scan strategy, and scan mirror thermal radiation interference still exists. Therefore, accurately identifying and effectively compensating for this type of thermal

radiation interference is key to improving the stability of the instrument background radiation and the accuracy of brightness temperature calibration.

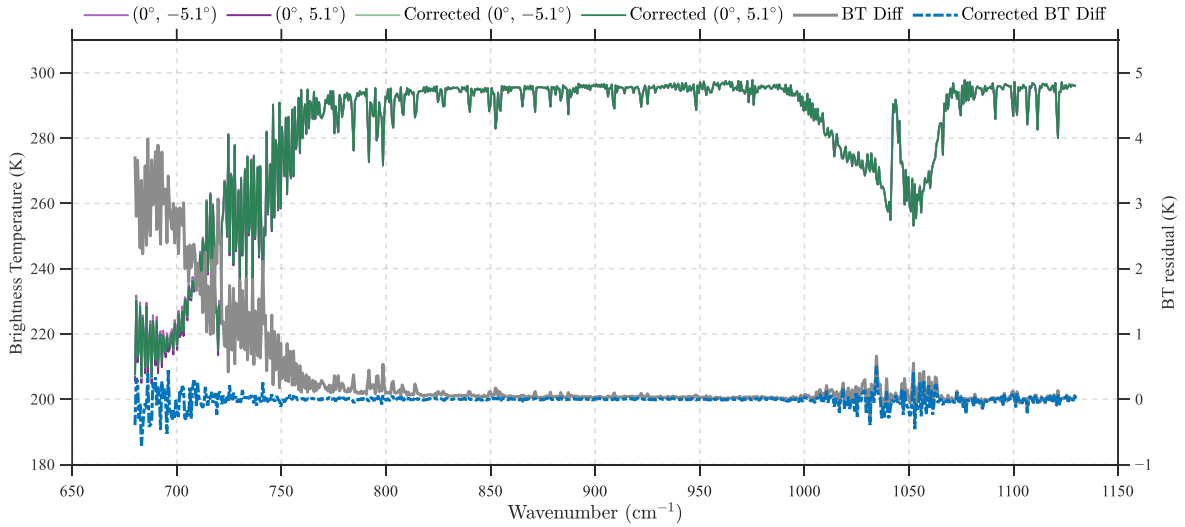


Figure 10. The impact of deep space observation position variation on ES calibrated brightness temperature. The purple and green curves represent the ES spectral brightness temperature results after being processed by the two-point calibration model, using different deep space observation positions as the deep space reference. The gray curve represents the brightness temperature jump, and the blue dotted line represents the corrected brightness temperature jump.

4. Discussion

4.1. Thermal Response Modeling of Scan Mirror Coefficients Based on Random Forest Regression

When the temperature-field is stable, the scan mirror surface temperature can be approximated as a constant. In this case, the background radiation disturbance induced by a unit change in scan angle tends to become stable, and the corresponding scan mirror coefficients C_1 and C_2 can be treated as constants. However, during actual on-orbit operation, the instrument thermal environment is subject to pronounced diurnal fluctuations due to variations in solar illumination conditions and other factors, which in turn cause non-stationary fluctuations in the scan mirror surface temperature. This temperature uncertainty renders the scan mirror coefficients time-dependent, thereby degrading the compensation accuracy and applicability of fixed-coefficient models across different time periods.

Since the scan mirror surface temperature cannot be directly obtained, the instrument temperature-field information is used as an indirect indicator of the scan mirror temperature. Therefore, this study introduces random forest regression to establish a nonlinear mapping between the instrument temperature-field and the scan mirror coefficients. This approach can characterize the complex nonlinear radiative transfer pathways between the instrument temperature-field and the scan mirror surface temperature, thereby enabling temperature-field-driven adaptive estimation and compensation of the coefficients. This method not only effectively compensates for the temperature-field-induced temporal variability of the scan mirror coefficients, but also offers the following advantages. First, random forest regression maintains strong nonlinear fitting capability even under medium- and small-sample conditions, and can adaptively capture the complex nonlinear impact of temperature-field variations on the scan mirror coefficients. Second, random forests exhibit low sensitivity to outliers and noise. By integrating the predictions of multiple decision trees, the ensemble algorithm significantly reduces the risk of overfitting and ensures the robustness of the model. Third, random forest modeling is straightforward and does not require complex feature engineering, as it can model directly in the original feature space,

thereby improving modeling efficiency. Finally, random forests provide good interpretability: feature importance evaluation can be used to identify the key physical variables that govern the scan mirror thermal radiation response, thus providing data-driven theoretical support for subsequent temperature-field modeling and on-orbit compensation [19].

Random forest is a typical nonlinear regression ensemble algorithm that constructs multiple mutually independent decision trees and aggregates the outputs of these trees for prediction, thereby enhancing the robustness and generalization capability of the model. Its training mechanism is based on the Bootstrap aggregating strategy, that is, M subsets are randomly drawn with replacement from the original samples, and each subset is used to train a corresponding decision tree. During tree construction, a random feature subspace selection mechanism is adopted, whereby N′ features are randomly selected from the N input features at each node for split evaluation. Finally, by aggregating the outputs of all decision trees, the random forest yields the system radiation response variations induced by unit scan-angle changes during the east–west and north–south scan mirror motions, respectively:

$$C_1(T_Field) = RF_{ew}(T_Field) \tag{11}$$

$$C_2(T_Field) = RF_{ns}(T_Field) \tag{12}$$

where $C_1(T_Field)$ and $C_2(T_Field)$ represent the east–west and north–south scan mirror coefficients, respectively, under the current instrument temperature field T_Field. RF_{ew} and RF_{ns} are the nonlinear regression models established for the east–west and north–south scan mirrors, respectively. By combining Equation (8), we can derive the system response variation $f(\Delta x, \Delta y, T_Field)$ caused by scan mirror deflection under the current temperature field:

$$f(\Delta x, \Delta y, T_Field) = C_1(T_Field) \times \Delta x + C_2(T_Field) \times \Delta y \tag{13}$$

Furthermore, by combining Equation (10), we can derive the on-orbit radiometric calibration model that removes the thermal radiation effects of the scan mirror at any given time, based on the current instrument temperature field information:

$$L_p^{ES}(T_Field) = \frac{S_p^{ES}(T_Field) - S_p^{DS}(T_Field)}{R_p(T_Field)} + L_{CBB} \tag{14}$$

This method adaptively updates the scan mirror coefficients to cope with different temperature-field conditions, thereby overcoming the limitations of relying on calibration parameters obtained from dedicated experiments. Meanwhile, based on feature importance, it can identify the key thermal environment factors, providing data-driven evidence for subsequent temperature-field modeling and instrument design.

4.2. Temperature-Field-Driven Scan Mirror Thermal Radiation Interference Correction Model

The preceding analysis has demonstrated that the scan mirror thermal radiation interference intensity is strongly correlated with the instrument temperature-field, and that the two exhibit highly synchronized variation characteristics in the temporal dimension. This indicates that static scan mirror coefficients obtained solely from dedicated deep space experiments cannot be directly extrapolated for use under different times or thermal conditions. To achieve dynamic compensation and quantitative correction of scan mirror thermal radiation interference, this study introduces random forest regression, using the temperature-field state as input variables to establish a nonlinear mapping model between the instrument temperature-field characteristics and the scan mirror coefficients. In this way, real-time estimation of scan mirror thermal radiation interference can be achieved, thereby improving the system radiometric calibration accuracy and response consistency.

In this paper, 4949 groups of deep space observation experiment data acquired from 19 September to 11 October 2022 are selected, and the temperature characteristics of the instrument's effective temperature measurement points are used to construct the aforementioned nonlinear mapping model. Meanwhile, to objectively evaluate the contribution of the temperature characteristics at different temperature measurement points to the prediction of the scan mirror coefficients, the Pearson correlation coefficient (PCC) between the temperature at each measurement point and the east–west and north–south scan mirror coefficients, as well as the model-derived feature importance (MDFI), are computed separately. On this basis, an integrated feature evaluation score (IFES) that combines physical correlation and model contribution is constructed, with higher weights assigned to emphasize the feature-driven contribution, so as to comprehensively assess the importance of each temperature measurement point. Through IFES evaluation, the key temperature measurement points that indicate the state variation in scan mirror thermal radiation interference are further identified (see Table 1, which lists only the top 15 temperature measurement points).

Table 1. Correlation, Feature Importance, and Integrated Effectiveness Score of Temperature Field Features.

No.	IFES	EW PCC	NS PCC	EW MDFI	NS MDFI
TMP-1	0.92	0.68	0.79	0.47	0.78
TMP-2	0.68	0.34	0.48	1.05	0.69
TMP-3	0.66	0.64	0.71	0.33	0.54
TMP-4	0.62	0.69	0.64	0.52	0.54
TMP-5	0.61	0.69	0.64	0.58	0.53
TMP-6	0.60	0.63	0.66	0.27	0.51
TMP-7	0.60	0.12	−0.05	0.94	0.86
TMP-8	0.54	0.70	0.62	0.84	0.47
TMP-9	0.52	0.62	0.40	0.49	0.57
TMP-10	0.51	0.35	0.51	0.48	0.49
TMP-11	0.50	0.54	0.48	0.35	0.50
TMP-12	0.48	0.66	0.58	0.34	0.42
TMP-13	0.48	0.26	0.27	0.65	0.60
TMP-14	0.46	0.68	0.62	0.50	0.37
TMP-15	0.45	0.59	0.72	0.46	0.30

4.2.1. Validation of the Generalization Performance of the Scan Mirror Thermal Radiation Interference Correction Model

To verify the generalization capability and robustness of the proposed model outside the training period, on-orbit observation data from 14–16 January 2022 were selected as an independent test set to evaluate the applicability of the model under thermal conditions that differ significantly from those of the training data. As shown in Figure 11, within the scan mirror thermal radiation interference–sensitive band (680.04–790.63 cm^{-1}), the actual system response changes induced by scan mirror deflection agree well with the fitted results (R^2 = 0.9784, root-mean-square error (RMSE) = 183.75), confirming the effectiveness and practical potential of predicting and compensating scan mirror thermal radiation disturbance based on temperature-field features.

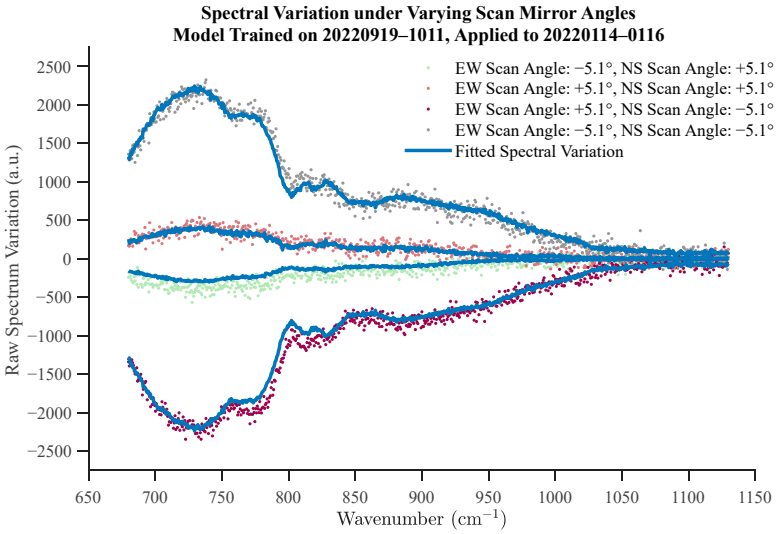


Figure 11. Comparison of deep space spectrum DN changes caused by scan mirror angle variations and model fitting results from 14 to 16 January 2022. The scatter points in different colors represent the spectral disturbances corresponding to different scan mirror angle variation combinations under actual measurement conditions, and the blue solid line represents the fitted disturbance curve predicted based on temperature features. "+" and "−" represent the positive and negative deflections of the scan mirror, respectively.

Further analysis and validation were carried out from the perspective of temporal continuity. Under ideal conditions, if scan mirror deflection does not introduce additional radiation interference, then, because the instrument's internal temperature-field is a continuous variable, the DS spectrum that characterizes the instrument background radiation should exhibit a smooth variation in time. Meanwhile, the diurnal variation in the DS observation spectrum should remain highly consistent with that of the ICT observation spectrum.

Figure 12 shows the temporal evolution of the DN values of the deep space spectrum at 729.53 cm^{-1} in the independent test set. During this period, a total of 20 scan mirror angle state switches occurred, and each switch was accompanied by a jump in the DSS signal, which was particularly pronounced when the east–west and north–south scan mirrors deflected in the same direction. By applying the temperature-field-driven model developed in this study to compensate for radiation disturbance, the jumps induced by scan mirror deflection were effectively suppressed, and the DSS time series became continuous and smooth.

The results in Figure 13 show that, after the correction of scan mirror thermal radiation interference, the diurnal variation curve of the DSS becomes highly consistent with that of the ICT observation spectrum in its temporal evolution, indicating that the model not only effectively removes scan mirror thermal radiation interference but also enhances the spectral response consistency among different observation modes.

The above validation demonstrates that the proposed temperature-field-driven nonlinear correction model effectively enhances the temporal generalization capability of the calibration strategy. This model provides essential support for achieving adaptive correction of scan mirror thermal radiation interference for spaceborne Fourier spectrometers, and lays a theoretical and methodological foundation for developing a high-accuracy and highly adaptive radiometric calibration system.

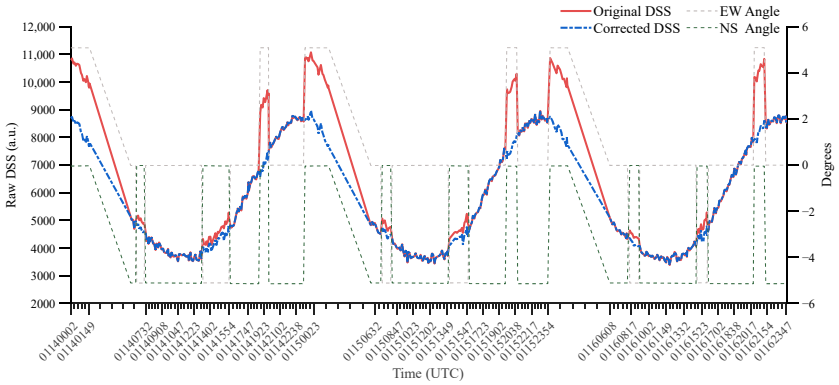


Figure 12. Time series variation in DSS DN at the wavenumber of 729.53 cm^{-1}. The red solid line represents the original uncorrected DSS curve, and the blue dashed line represents the DSS result after scan angle difference compensation. The gray dashed line and the green dashed line represent the angle states of the east–west and north–south scan mirrors, respectively.

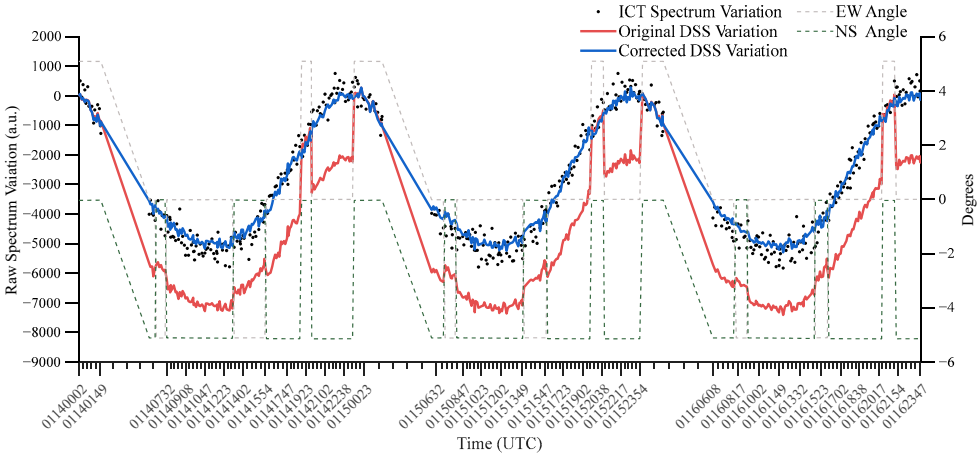


Figure 13. Comparison of deep space spectrum diurnal variation trends before and after scan mirror angle disturbance correction with the ICT spectrum. The red solid line represents the original DSS DN diurnal variation curve over time, and the blue curve represents the DSS DN diurnal variation curve after scan angle difference compensation. The black scatter points represent the diurnal variation in the ICT spectrum. The gray dashed line and the green dashed line represent the angle states of the east–west and north–south scan mirrors, respectively.

4.2.2. O–B Validation Based on a Radiative Transfer Model

To evaluate the effectiveness of the radiation interference correction for small scan mirror attitude changes under a fixed deep space reference source position, this study performs a validation using the radiative transfer simulation model RTTOV. The experiment selects the Bay of Bengal region, where clear-sky ocean scenes are densely distributed in March 2024, and applies a clear-sky detection algorithm to screen high-quality cloud-free samples. On this basis, the scan mirror thermal radiation disturbance correction is applied to the data over the selected region, and the calibration stability before and after the correction is quantitatively analyzed.

Figure 14 shows the improvement in the standard deviation of Observation minus Background (O–B) before and after the correction. The results show that, after compensating for the scan mirror thermal radiation disturbance, the maximum reduction in the O–B standard deviation is about 0.15 K. It is worth emphasizing that this correction experiment only addresses the radiative interference induced by scan mirror deflection, without incorporating any additional calibration optimization methods, and that, in the selected dataset, the deep space reference source position is fixed and the scan mirror angle variation

range is limited. When the scan mirror angle variation range is further enlarged, a more pronounced improvement in the stability of O–B after correction can be expected.

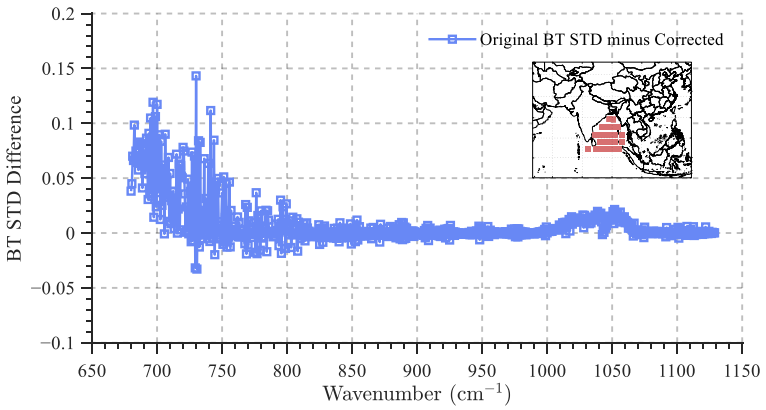


Figure 14. Change in O-B calibration relative standard deviation after scan mirror thermal radiation interference correction in the longwave channel. The inset in the upper right corner shows a schematic of the selected observation scene.

4.3. Future Work and Outlook

High-accuracy radiometric calibration is a critical prerequisite for ensuring the quality of remote sensing retrieval products; therefore, constructing a systematic and rigorous radiometric calibration framework is of particular importance. In this study, a dynamic correction model is developed to address scan mirror thermal radiation interference, providing a theoretical and methodological basis for further improving radiometric calibration accuracy. However, the current work still has several limitations, which need to be further refined and validated in future studies.

First, previous studies have shown that the calibration accuracy of certain GIIRS channels exhibits diurnal variation characteristics, suggesting that variations in the instrument temperature-field may be one of the causes of this system bias. Because the scan mirror adopts different attitudes in the ES, DS, and ICT observation modes, different observation modes will, in principle, introduce scan-angle-dependent response differences governed by the instrument temperature-field, thereby leading to a certain degree of diurnal variation in calibration accuracy. Therefore, future work should, within the existing correction framework, assess the capability of scan mirror thermal radiation interference compensation to suppress the diurnal variation characteristics of GIIRS products [20]. At the same time, longer time series and multi-scene datasets should be incorporated to quantitatively evaluate the improvement brought by this correction to the accuracy of end-to-end calibrated products.

Secondly, the frequency of temperature field and internal calibration target spectra acquisition in existing on-orbit experiments is limited, and the temporal resolution is insufficient, making it difficult to accurately characterize the time-varying process of the instrument's background radiation and support the fine time-varying representation of the temperature-field-driven correction model. In the future, the adaptability of the model to non-stationary thermal environments can be enhanced by increasing the measurement frequency of temperature and radiance. Finally, the present work mainly focuses on correcting the interference introduced by the polarization response of scan mirror self-emission. Future studies will further incorporate the polarization effects of entrance-pupil radiation and consider their coupling with scan mirror self-emission, with the aim of developing a more complete and higher-accuracy radiometric calibration model and thereby forming a more robust and adaptive radiometric calibration framework.

5. Conclusions

In this study, a systematic analysis is carried out of the systematic bias induced by scan mirror deflection in the GIIRS instrument onboard the FY-4B satellite. Focusing on scan mirror thermal radiation interference, we conduct mechanism analysis, thermal radiation response modeling, and develop a temperature-field-based adaptive compensation method, which is validated using on-orbit measurement data, leading to the following important scientific findings and innovative results.

First, based on deep space observation data, this study reveals the formation mechanism of scan mirror thermal radiation interference and, on this basis, constructs a scan mirror thermal radiation interference correction model tailored to GIIRS. The coupling mechanism between scan mirror self-emission and the system polarization response is systematically clarified, providing theoretical support and methodological guidance for subsequent calibration and compensation.

Second, this study innovatively proposes a temperature-field-driven adaptive interference compensation method. This method introduces a nonlinear mapping relationship between scan mirror thermal radiation interference and the instrument temperature-field and establishes a dynamic modeling and real-time compensation framework based on machine learning. Its key advantage is that it does not rely on pre-set experimental parameters; bias correction can be achieved using only on-orbit temperature measurements, demonstrating high engineering feasibility and methodological scalability.

On this basis, we verify the practical performance of the proposed method using independent on-orbit datasets. The results show that the background radiation interference induced by scan mirror deflection is effectively suppressed, and in the O–B test the maximum improvement in the relative standard deviation is about 0.15 K. Specifically, after correction, the diurnal variation consistency between deep space and blackbody spectra is significantly improved; during deep space observations, the relative radiation fluctuation amplitude in the interference-sensitive channel at 729.53 cm^{-1} is reduced from 78.82% to 7.70%. Over the full longwave channel spectrum, the standard deviation of the deep space system response decreases from a maximum of 1260 DN to below 130 DN. In addition, the mean radiance bias is reduced from 1 $mW \cdot m^{-2} \cdot sr^{-1} \cdot cm^{-1}$ to 0.06 $mW \cdot m^{-2} \cdot sr^{-1} \cdot cm^{-1}$, and the standard deviation of the radiance bias decreases from a maximum of 2.5 $mW \cdot m^{-2} \cdot sr^{-1} \cdot cm^{-1}$ to below 0.5 $mW \cdot m^{-2} \cdot sr^{-1} \cdot cm^{-1}$, indicating that the proposed method can effectively remove system bias and significantly enhance on-orbit stability and response consistency among observation modes.

Finally, by combining physical mechanism analysis with data-driven methods, this study proposes a temperature-field-driven adaptive correction scheme for scan mirror thermal radiation interference, providing a solid theoretical foundation and a feasible implementation pathway for high-accuracy calibration and long-term stable operation of geostationary-orbit infrared hyperspectral payloads. This scheme not only optimizes the existing calibration model but also exhibits good engineering applicability and strong potential for extension, and is particularly suitable for high-accuracy remote sensing missions under complex thermal environments.

Author Contributions: Conceptualization, X.L.; Methodology, X.L., Y.Z. (Yaopu Zou) and P.H.; Software, X.L.; Validation, X.L. and P.H.; Formal analysis, X.L.; Investigation, X.L.; Resources, C.H. and L.L.; Data curation, Y.Z. (Yaopu Zou), C.H. and Y.Z. (Yuanshu Zhang); Writing—original draft, X.L., Y.Z. (Yaopu Zou) and C.H.; Writing—review & editing, X.L.; Visualization, X.L.; Supervision, Y.Z. (Yuanshu Zhang), C.H. and L.L.; Project administration, Y.Z. (Yaopu Zou), C.H., L.L. and Y.Z. (Yuanshu Zhang); Funding acquisition, Y.Z. (Yaopu Zou) All authors have read and agreed to the published version of the manuscript.

Funding: This research was funded by the Youth Innovation Promotion Association, Chinese Academy of Sciences (CAS), (grant number 2023252).

Data Availability Statement: The datasets generated and analyzed during the current study are available from the corresponding author upon reasonable request.

Acknowledgments: The authors would like to express their sincere appreciation to the National Satellite Meteorological Centre (NSMC) for its valuable support.

Conflicts of Interest: The authors declare no conflict of interest.

References

1. Zeng, Z.-C.; Lee, L.; Qi, C. Optimal estimation retrieval of tropospheric ammonia from the Geostationary Interferometric Infrared Sounder onboard FengYun-4B. *Atmos. Meas. Tech. Discuss.* **2023**, *16*, 3693–3713. [CrossRef]
2. Zeng, Z.-C.; Lee, L.; Qi, C. Diurnal carbon monoxide observed from a geostationary infrared hyperspectral sounder: First result from GIIRS on board FengYun-4B. *Atmos. Meas. Tech.* **2023**, *16*, 3059–3083. [CrossRef]
3. Pagano, T.S.; Aumann, H.H.; Overoye, K.; Gigioli, G.W., Jr. Scan-angle-dependent radiometric modulation due to polarization for the Atmospheric Infrared Sounder (AIRS). In Proceedings of the Earth Observing Systems V, San Diego, CA, USA, 15 November 2000; pp. 108–116.
4. Taylor, J.K.; Revercomb, H.E.; Tobin, D.C. An analysis and correction of polarization induced calibration errors for the cross-track infrared sounder (CrIS) sensor. In Proceedings of the Fourier Transform Spectroscopy, Singapore, 5–8 November 2018; p. FW2B.3.
5. Wu, C.; Qi, C.; Hu, X.; Gu, M.; Yang, T.; Xu, H.; Lee, L.; Yang, Z.; Zhang, P. FY-3D HIRAS radiometric calibration and accuracy assessment. *IEEE Trans. Geosci. Remote Sens.* **2020**, *58*, 3965–3976. [CrossRef]
6. Weinreb, M.; Jamieson, M.; Fulton, N.; Chen, Y.; Johnson, J.X.; Bremer, J.; Smith, C.; Baucom, J. Operational calibration of Geostationary Operational Environmental Satellite-8 and-9 imagers and sounders. *Appl. Opt.* **1997**, *36*, 6895–6904. [CrossRef] [PubMed]
7. Xiong, X.; Sun, J.; Wu, A.; Chiang, K.-F.; Esposito, J.; Barnes, W. Terra and Aqua MODIS calibration algorithms and uncertainty analysis. In Proceedings of the Sensors, Systems, and Next-Generation Satellites IX, Bruges, Belgium, 21 October 2005; pp. 255–264.
8. Xiong, X.; Chiang, K.; Chen, N.; Xiong, S.; Barnes, W.; Guenther, B. Results and lessons from MODIS thermal emissive bands calibration: Pre-launch to on-orbit. In Proceedings of the Earth Observing Systems XI, San Diego, CA, USA, 7 September 2006; pp. 85–96.
9. Chiang, K.-F.; Xiong, X. Pre-launch characterization of aqua MODIS scan mirror response versus scan angle for thermal emissive bands. In Proceedings of the Earth Observing Systems XII, San Diego, CA, USA, 27 September 2007; pp. 559–571.
10. Li, X.; Wang, B.; Wu, Y.; Han, C.; Cao, Q.; Zhou, S.; Wang, W.; Li, P. Study on the improvement of scan mirror thermal radiation correction on the calibration accuracy of FY-4A AGRI. *J. Infrared Millim. Waves* **2022**, *41*, 608–617.
11. Oudrari, H.; McIntire, J.; Xiong, X.; Butler, J.; Lee, S.; Lei, N.; Schwarting, T.; Sun, J. Prelaunch radiometric characterization and calibration of the S-NPP VIIRS sensor. *IEEE Trans. Geosci. Remote Sens.* **2014**, *53*, 2195–2210. [CrossRef]
12. Guenther, B.; Xiong, X.; Barnes, W.L.; Murphy, R.E. A calibration algorithm design and analysis for VIIRS thermal emissive bands based on the EOS MODIS approach. In Proceedings of the IGARSS 2003, 2003 IEEE International Geoscience and Remote Sensing Symposium, Proceedings (IEEE Cat. No. 03CH37477), Toulouse, France, 21–25 July 2003; pp. 3036–3038.
13. Datla, R.; Shao, X.; Cao, C.; Wu, X. Comparison of the calibration algorithms and SI traceability of MODIS, VIIRS, GOES, and GOES-R ABI sensors. *Remote Sens.* **2016**, *8*, 126. [CrossRef]
14. Li, L.; Ni, Z.; Qi, C.; Yang, L.; Han, C. Pre-launch radiometric calibration of geostationary interferometric infrared sounder on FengYun-4B satellite. *Acta Opt. Sin.* **2022**, *42*, 0630001. [CrossRef]
15. Zou, Y.P.; Feng, X.; Han, C.P.; Li, L.B.; Liang, X. Research on nonlinear correction algorithm of Fourier transform spectrometer based on responsivity correction. *J. Infrared Millim. Waves* **2023**, *42*, 369–376.
16. Zhu, Y.; Xin, S.; Chen, X.; Song, J.; Gu, M. Uncertainty Model for Emissivity Measurement of Blackbody on Infrared Absolute Radiance Payload Based on Heated Halo Structure. *Acta Opt. Sin.* **2025**, *45*, 1012002.
17. Niu, J.; Li, F.; Ma, L. The theoretical analysis of thermal infrared emission polarization and experimental verification. *Opto-Electron. Engin.* **2014**, *41*, 88–93.
18. Liu, C.; Xiong, D.; Dong, Y. Optimization of temperature measurement of infrared radiation via theory of radiant heat transfer angle coefficient. *Chin. J. Quantum Electron.* **2019**, *36*, 490–494.

19. Tripathi, R.; Tripathy, B.R.; Jena, S.S.; Swain, C.K.; Mohanty, S.; Sahoo, R.; Nayak, A. Prediction of rice yield using sensors mounted on unmanned aerial vehicle. *Agric. Res.* **2024**, *14*, 835–845. [CrossRef]
20. Yin, R.; Han, W.; Gao, Z.; Di, D. The evaluation of FY4A's Geostationary Interferometric Infrared Sounder (GIIRS) long-wave temperature sounding channels using the GRAPES global 4D-Var. *Q. J. R. Meteorol. Soc.* **2020**, *146*, 1459–1476. [CrossRef]

Disclaimer/Publisher's Note: The statements, opinions and data contained in all publications are solely those of the individual author(s) and contributor(s) and not of MDPI and/or the editor(s). MDPI and/or the editor(s) disclaim responsibility for any injury to people or property resulting from any ideas, methods, instructions or products referred to in the content.